Smart hybrid composite sensor technology to enhance the detection of low energy impact damage in composite structures

Sakineh Fotouhi[1], Meisam Jalalvand[2], Michael R Wisnom[3], Mohammad Fotouhi[4*]

[*] m.fotouhi-1@tudelft.nl

[1] University of Glasgow, Glasgow G12 8QQ, UK
[2] Engineering Materials, School of Engineering, University of Southampton, Southampton, SO17 1BJ, UK
[3] Bristol Composites Institute, University of Bristol, Bristol BS8 1TR, UK
[4] Faculty of Civil Engineering and Geosciences, Delft University of Technology, Delft, 2628 CD, Netherlands

Abstract

This paper introduces novel structural health monitoring (SHM) sensors to improve the detection of low energy impact damage in laminated composites. The sensor is a purposely designed thin-ply hybrid composite, composed of a layer of unidirectional S-glass/epoxy and another layer of unidirectional ultra-high modulus (UHM) carbon/epoxy. The sensor was incorporated onto both the impacted face and back of a substrate plate made from unidirectional T800 carbon/MTM49-3 epoxy prepregs with the stacking sequence of $[45/0/90/-45]_{4S}$. A series of drop tower tests were conducted on the composite plates with and without the attached hybrid sensing layer, with two different in-plane dimensions and varying energy levels ranging from 3J to 124J. The results indicate that the sensors functioned satisfactorily and provided direct correlations between visible and internal hidden damage detected by C-scan. The sensor can be optimized by selecting appropriate material properties and adjusting it to the in-plane dimensions of the substrate.

Keywords: Impact damage, Structural health monitoring, Carbon fibre composite, Hybrid composites.

1. Introduction

Due to advantageous properties of composite materials such as light weight and high strength-to- weight ratio, the demand for these materials is rapidly increasing. Composites are now widely used for aerospace, automotive, marine, construction, consumer goods, and more. For example, 50% of structural weight in the Boeing 787 Dreamliner is fibre reinforced composite [1]. However, a crucial limitation of current composite laminates that remains unresolved is their vulnerability to impact damage [2]. Detecting damage visually is a major challenge for carbon/epoxy composite laminates since such materials are susceptible to impact

damage, including delamination and backside fiber breakage, which may not be visible at the site of the impact. The mechanical properties of laminates can be greatly affected by Barely Visible Impact Damage (BVID), causing a reduction in compressive strength of up to 60% when compared to an undamaged laminate [3,4]. As a result, very large design margins and more technical maintenance and inspection procedures are required compared to metallic structures.

Due to the significant impact of BVID on the performance and safety of composite aircraft, the inspection and monitoring of BVID is one of the most extensively researched areas of aerospace composites. Detecting damage, in safety critical composite structures such as aircrafts, is necessary, but it is a very expensive and labour-intensive process [5,6]. Visual Inspection (VI) by a skilled person is the most common and expedient method to find cracks or surface dents in safety critical structures such as composites [7,8]. For example, VIs account for over 80% of inspections performed on large transport category aircraft [9]. However, VI heavily depends on the operator's skills, and there is an increasing need to cover large areas of structure that are usually not easy to access, therefore increasing the cost, errors, and health and safety (H&S) risks [10]. For examples, VI for large aircraft may require up to 40000 hours [11], and the most common practices of VI include access by lift platforms for airplanes and rope access for wind turbine blades. BVID is usually found in noisy backgrounds due to the texture of composite materials, which lead to poor VI reliability. As a result, VI is not reliable enough for small damage, as shown in Fig. 1, and complex and expensive special detailed inspection procedures such as ultrasonic, shearography and thermographic techniques are necessary to ensure the safety and reliability of composite structures [7]. Various methods such as C-scanning and CT-scanning [12], electrical resistant measurement [13], acoustic emission monitoring [14], and fibre bragg gratings [15] have been suggested and tested as a means of capturing impact events and tracking the evolution of resultant damage. All these methods, require electrical wiring, power, operator interpretation of data and can be less reliable in complex structures, which are barriers to industrial implementation.

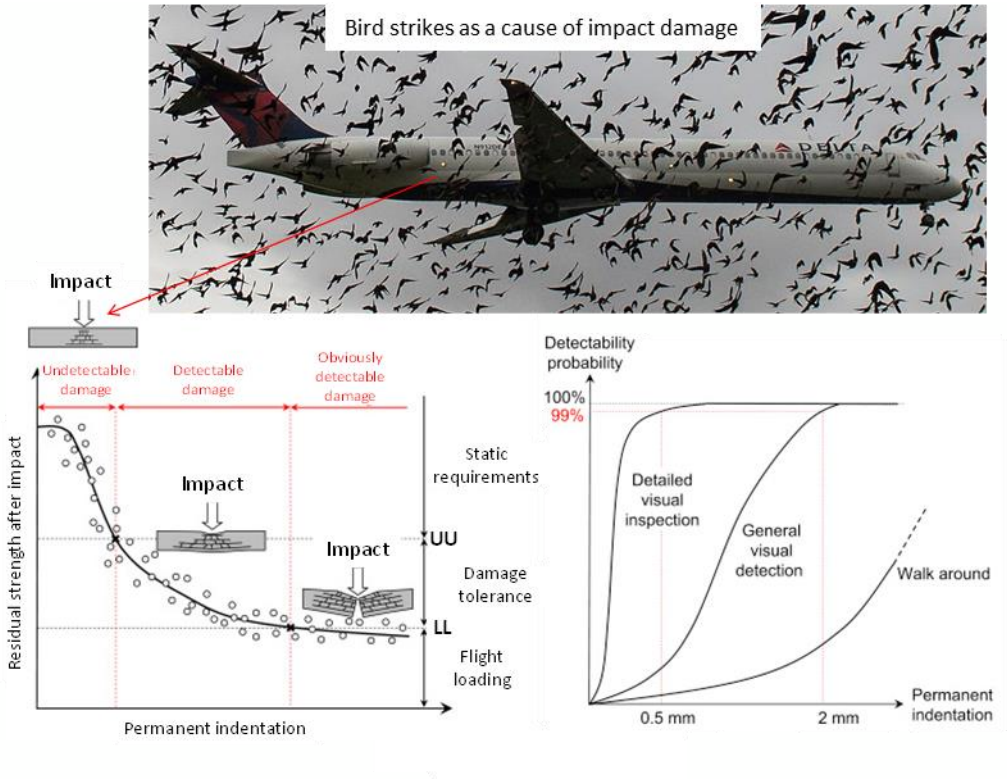

Fig. 1. Impact damage in composite laminates, left: the effect on residual strength, right: probability of detection [9].

Self-sensing composites are emerging technologies that have the ability to detect their own physical conditions, including stress, strain, temperature, deformation, and damage [16]. Changes in colour, fluorescence, or production of luminescence can provide visual indications of damage and deformation in self-sensing fiber-reinforced composites. This is accomplished by integrating dye-filled capsules, hollow fibers, or microchannels into damage-indicating coatings or embedding them into the composite, either within the polymer resin or at the interface between fibers and polymer resin [17,18]. When the reservoirs rupture, their contents flow into cracks and voids, thus revealing their location. The synthesis of materials with intrinsic mechanochromic properties is a second strategy, in which the polymer matrix or the surface of the fibers is functionalized with functional groups or additives that can alter their optical appearance in response to mechanical deformation [19-21]. A drawback of these damage detection systems is that detecting the signals and processing data necessitates the use of specialized equipment. As a result, they are time-consuming, costly and they require skilled people for evaluation.

Overall, the literature reveals that the reduction in strength resulting from BVID remains a significant and unresolved limitation of current composite laminates which results

in very large design margins and more technical maintenance procedures. Therefore, there is the need to develop improved and more efficient means of detecting damage. A recent study [22] proposed a novel purpose-built interlayer composite sensor composed of thin glass and carbon-epoxy hybrid prepregs. When subjected to tension beyond a specified strain value, this hybrid composite changes its appearance, indicating an overload of the structure. The idea of this paper is to introduce novel hybrid composites with visible damage to improve the reliability of damage detection. This contrasts with the use of attached or embedded sensors, which are more costly, difficult to deploy and less durable than the structural material (see Fig. 2). These hybrid sensing layers act both as a load carrying component and a damage indicator and are completely wireless and offer low-cost and simple solutions for damage detection. The system developed is best suited as an early warning tool for the first inspection of composite structures. The proposed technology can therefore replace or complement current commercial inspection tools to make composite structures more durable while ensuring safety.

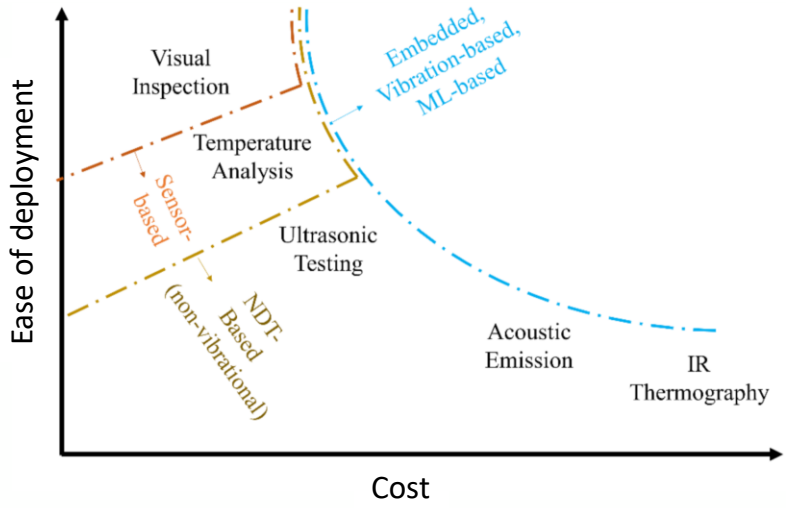

Fig. 2. A comparison of different inspection methods shows that visual inspection is the quickest and cheapest inspection method [23].

2. Design principles of the sensor

The idea of this sensing technology is simple: a glass/carbon hybrid composite is integrated during manufacturing (or can be attached afterwards) on top of the carbon/epoxy composite substrate as shown in Fig. 3. The plate surface is fully black when it is initially manufactured. This is because the glass layer is translucent so light passes through and gets completely absorbed by the black opaque carbon layer. When the plate is subjected to impact,

there is carbon fracture followed by (1) an incremental crack growth at the carbon/glass interface and (2) splits in the glass layer along the fibres, as shown in Fig. 3(b). This damage scenario acts as a barrier to the light and reflects it back so brighter marks will be visually detectable. The size of visible damage on the impacted side is proportional to the level of impact energy.

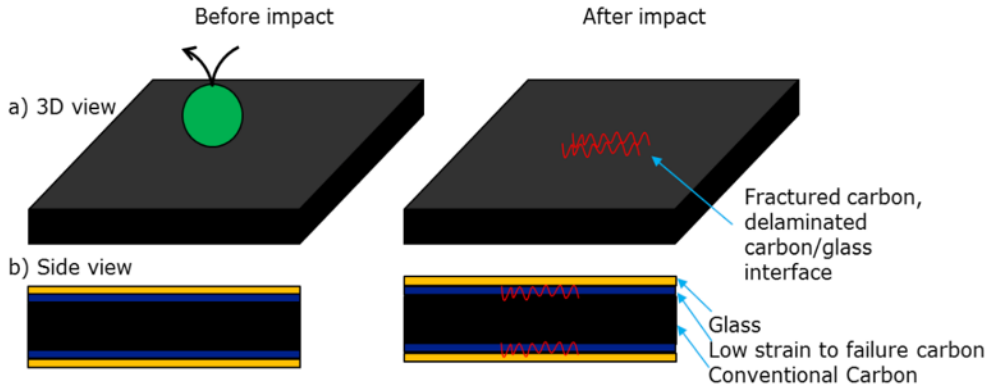

Fig. 3. a) Schematic 3D and b) side views of a carbon/epoxy composite with the impact detector hybrid composite sensors.

The hybrid sensor design, i.e. selection of the thickness, materials and layup, is done by calculating the critical load levels for the three failure mechanisms of mid-plane delamination, back-face tensile fibre failure and impacted side fibre failure in a laminate under low-velocity impact, using equations 1, 5 and 7. These equations can be implemented simultaneously to determine the competition between the main damage modes. The idea is to prevent mid-plane delamination damage as the first damage mode and instead trigger fibre failure in the low strain sensor material as the first active mode.

Mid-plane delamination: The critical load for initiation of midplane delamination (F_C) can be calculated by equation 1, reported by Davis [24].

$$F_{C\,th}^2 = \frac{8\pi^2 E(2t)^3}{9(1-\vartheta^2)} G_{IIC} \qquad (1)$$

where E, t, ν and G_{IIC} are bending modulus, thickness, Poisson ratio and critical strain energy in mode II delamination, respectively.

The stresses caused by a Hertzian contact load on a transversely isotropic circular plate can be defined by equations 2 and 3 [25].

$$\sigma_{zz}(0,z_0) = -p_0\left[1+\frac{S_1S_2}{S_1-S_2}\frac{z_0}{c}\left(arctan\frac{c}{S_1z_0}-arctan\frac{c}{S_2z_0}\right)\right] \quad 2$$

$$\sigma_{rr}(0,z_0) = -\frac{p_0}{S_1-S_2}\left[S_1\left(1/\sqrt{D}-\lambda p_2/2\right)\left(1-\frac{S_1z_0}{c}\arctan\frac{c}{S_1z_0}\right)\right.$$
$$\left.-S_2\left(1/\sqrt{D}-\lambda p_1/2\right)\left(1-\frac{S_2z_0}{c}\arctan\frac{c}{S_2z_0}\right)\right] \quad 3$$

Where

$$S_{1,2}^2 = \left(A+C\pm\sqrt{(A+C)^2-4D}\right)/2D$$
$$A = a_{13}\left(a_{11}-a_{12}\right)/Q$$
$$B = \left[a_{13}\left(a_{13}+a_{44}\right)-a_{12}a_{33}\right]/Q$$
$$C = \left[a_{13}\left(a_{11}-a_{12}\right)+a_{11}a_{44}\right]/Q$$
$$D = \left(a_{11}^2-a_{12}^2\right)/Q$$
$$Q = a_{11}a_{33}-a_{13}^2$$
$$p_1 = 1-AS_1^2$$
$$p_2 = 1-AS_2^2$$
$$\lambda = (B-1)\sqrt{D}/(AC-D)$$
$$\mu = (B-1)(A+\sqrt{D})/(AC-D)$$

In these equations, $z0 = z + h/2$, $p_0 = 3F/(2\pi c^2)$ and a_{ij} are compliance matrix terms, as defined by Lekhnitskii [26].

Back-face tensile fibre failure: Tensile fibre failure is the result of tensile normal stresses, and it usually occurs at the back of thin laminates, where the flexural tensile stresses are high. Considering maximum tensile stress (X_t) for fibre failure Equation 4, and solving for F, the fibre failure load can be evaluated.

$$\left(\frac{\sigma_{rr}}{X_t}\right)^2 \geq 1 \quad 4$$

Impacted side fibre failure: The compressive normal stress on the impacted side, which is responsible for compressive fiber failure, is the result of both bending and contact stresses.

Therefore, adding the stresses due to bending and contact from Equations 2 and 3 should be used to derive the critical stress for compressive fiber failure as expressed by equation 5.

$$\sigma_{rr}^{total} = \frac{3F}{2\pi^2(S_1 - S_2)}\left[S_1\left(1/\sqrt{D} - \lambda p_2/2\right)\left(1 - \frac{S_1 z_0}{c}\arctan\frac{c}{S_1 z_0}\right) - S_2\left(1/\sqrt{D} - \lambda p_1/2\right)\left(1 - \frac{S_2 z_0}{c}\arctan\frac{c}{S_2 z_0}\right)\right] + 6M_{rr}/h^2 \quad (5)$$

Using maximum tensile stress (X_c) for fiber failure in compression (Equation 6), critical load for compressive fiber failure can be extracted.

$$\left(\frac{\sigma_{rr}}{X_c}\right)^2 \geq 1 \quad (6)$$

3. Experimental methods

3.1. Manufacturing and material properties

As listed in

Table 1, three different types of laminates including reference (REF), an integrated S-glass/HS40-Carbon hybrid sensor laminate (HS40) and an integrated S-glass/YS-90A-Carbon hybrid sensor (YS-90) were investigated at two different scales. Schematics of the investigated samples and their dimensions are illustrated in Fig. 4. The REF laminate was a quasi-isotropic (QI) stacking sequence, $[45/0/90/-45]_{4s}$, which was made of a unidirectional T800 carbon/MTM49-3 epoxy prepreg. The plate was initially in the form of a 330 x 330 mm square, later, it was trimmed to create a rectangular test sample with nominal in-plane dimensions of 140 x 90 mm and a thickness of 4.64 mm. The direction of unidirectional fibre orientation that runs parallel to the long side of the plate is considered as 0°. The hybrid sensors, HS40 and YS-90, were integrated in the laminates and were cured at the same time as the core laminate, with the suppliers' recommended curing temperature of 120°C. Characteristics of the utilised prepregs are summarised in Table 2. The sensors were integrated in the front and back faces of the core laminate. Each sensor consisted of a single layer of HS40 or YS-90A carbon prepregs, positioned at 90° orientation, which was placed between the core laminate and a single layer of S-glass prepreg with a 90° orientation. If added on one side, the hybrid composite sensor adds around 4.5% extra thickness to the REF substrate laminate. However, in practical applications, the thickness of the substrate laminate is usually higher than in the current study, in addition, the hybrid composite sensor is a structural element, so once characterised, it can replace some final composite layers of the substrate in the manufacturing stage, causing no extra thickness/weight.

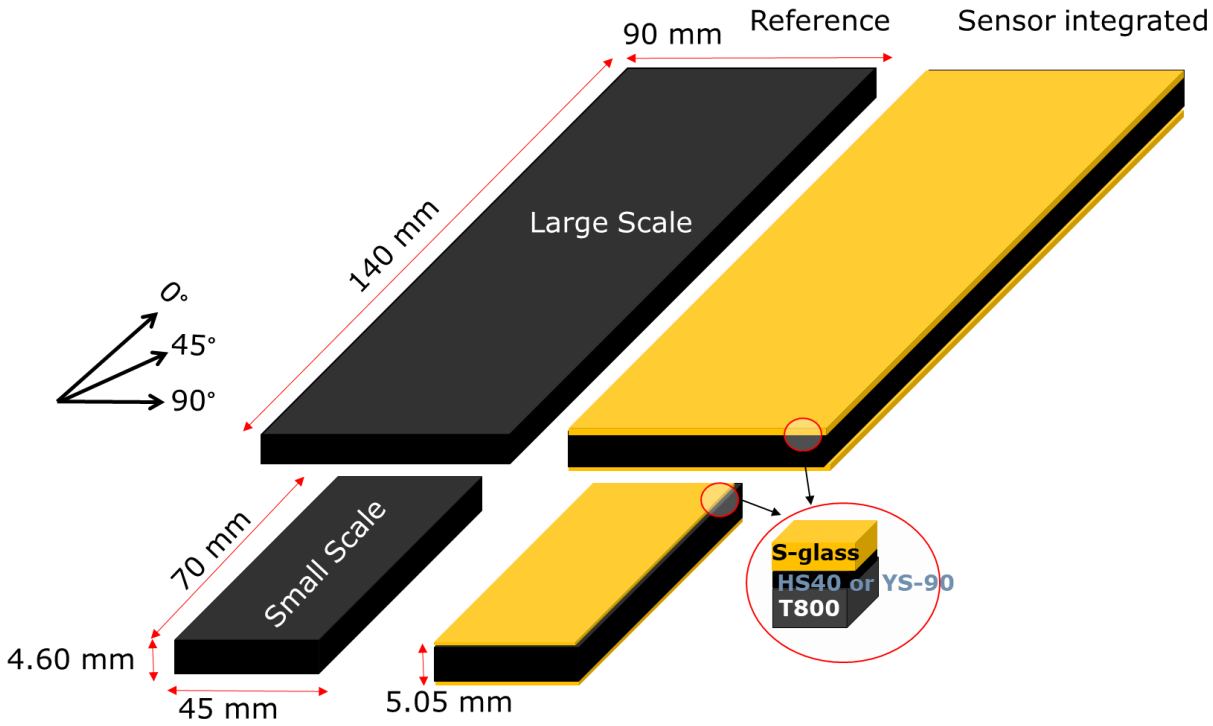

Fig. 4. Schematic of the reference (REF) and sensor integrated samples (HS40 and YS-90) with two different investigated scales. Both the small and large samples were cut from the same plate and had identical thicknesses.

Table 1. Configuration of the samples.

Sample's name	Layup	Materials
REF	$[45/0/90/-45]_{4S}$	QI T800
HS40	*90S-glass/90HS40/*$[45/0/90/-45]_{4S}$*/90HS40/90S-glass*	QI T800/HS-40/S-glass
YS-90	*90S-glass/90YS-90A/*$[45/0/90/-45]_{4S}$*/90YS-90A/90S-glass*	QI T800/YS-90A/S-glass

Table 2. Characteristics of the utilised pre-pregs.

Pre-preg type	**Cured nominal thickness (mm)**	**Tensile failure strain (%)**	**Compression strain to failure (%)**
T800/MTM49-3 epoxy [27]	0.145	1.70	1.5 [28]
S-glass/913 epoxy [29,30]	0.155	3.98	2.33[a]
HS40/epoxy (UPN069) [31,32]	0.07	1.00	-
YS-90A/epoxy (E9026A) [33]	0.07	0.30	-

[a] the calculations were made based on a 60% fibre volume fraction using data provided by the manufacturer.

3.2. Quasi-static indentation

Quasi-static indentation tests were first used to understand the behaviour of the investigated samples and to choose appropriate energy levels for the impact tests. Fig. 5 shows the experimental set-up used for the indentation tests and a typical load-displacement graph for the large scale REF laminate with different degrees of damage evolution experienced by the laminate. A steel indenter with 16 mm diameter was fitted on the Instron 8872 servo-hydraulic testing machine. ASTM D7136 standard [34] was used for the setup, where the indenter was forced against the rectangular sample, supported over a 125 × 75 mm window (for the large scale) and a 62.5 x 37.5 mm window (for the small scale), with 4 clamps, as shown in Fig. 5 (a). Displacement control with a feed rate of 2 mm/min was used to conduct the indentation tests. The area underneath the load-displacement graph, up to the first load drop, was calculated as the critical energy level for the damage initiation, and the total energy that can be absorbed before significant fibre failure in the laminate (up to the final load drop). Please note there were some fibre failures earlier than the main load drop, but those did not have a considerable effect on the load carrying capacity of the laminate. For the small scale samples, the final load drop was caused by free-edge delamination.

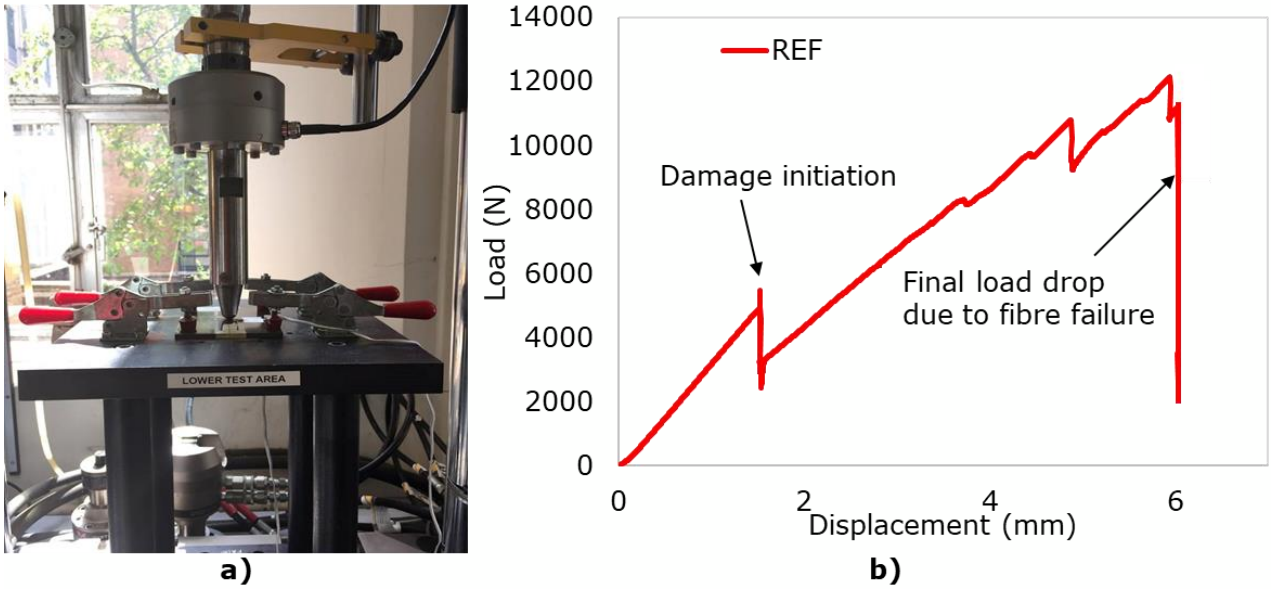

Fig. 5 (a) Experimental set-up for the quasi-static indentation test, (b) A representative load-displacement result for the large scale of a REF laminate.

3.3 Low-velocity impact

The ASTM D7136 standard [34] was followed to perform low-velocity impact tests using an Instron Dynatup 9250 HV drop-weight impact tower and a 16 mm diameter hardened

steel indenter (8 mm for the small scale) at various energy levels ranging from 3 J to 124 J. To support the large and small test samples, windows measuring 125 x 75 mm and 62.5 x 37.5 mm were used, respectively. Four rubber-tipped clamps were used to secure the samples, as shown schematically in Figure 6. A single accelerometer placed inside the tup measured the impact load and deflection, and a 4kHz filter in the console software was applied to the measured data to reduce noise and oscillations.

3.4 C-Scanning

After the indentation tests were done, the samples were C-scanned to observe the internal damage. A 10 MHz transducer was used to scan the samples in a water tank. USL Software was used to adjust the scanning parameters. The damage area was measured in the software and the results were then recorded.

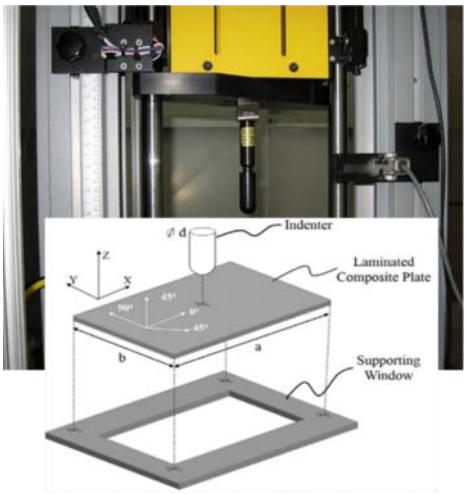

Fig. 6. Experimental configuration for the drop tower tests.

4. Experimental Results

The results from quasi-static indentation and low-velocity impact tests are analysed in this section to investigate the initiation of damage in the REF and sensor integrated samples. The correlation between visible surface damage and the magnitude of internal damage is investigated by comparing images from visual observation against C-scanning results.

4.1. Quasi-static indentation

Fig. 7 shows load-displacement plots obtained during the quasi-static indentation tests for the investigated samples. The large-scale samples were subjected to loading until fiber failure occurred at the back face due to tension, while for the small-scale samples, loading was stopped when free-edge delamination took place. The indented samples exhibit an elastic linear behaviour in the initial phase of the loading process, without any observable damage in the

laminate. After that there is a sudden first load drop that coincides with the onset and rapid growth of delamination at a number of different interfaces.

To investigate the strain behaviour of the samples experimentally, strain gauges with a 90° orientation are used to measure the strain level of the large samples in the centre on the back face, and on the front face at 10 mm distance from the centre, allowing enough space for the indenter while preventing it from damaging the strain gauge. The results of the load against time and strain versus time are illustrated in Fig. 8. Adding the hybrid sensor on the reference laminate does not have a significant effect on the strain distribution pattern before the initial load drop. But there is quite a difference in the strain measurements after the load drop, with different trends for the back and front face gauges. HS40 sample experienced the lowest strain levels after the load drop, and the REF sample had the highest strain level on the back face after the load drop. Fig. 8(a) shows that the strain level for the delamination initiation and the final fibre failure stages on the back face of the samples is about 0.9 % and higher than 2 %, respectively. The strain levels up to delamination initiation can be used to choose an appropriate grade of the carbon and glass layers for the hybrid sensor to be activated at a desired strain level.

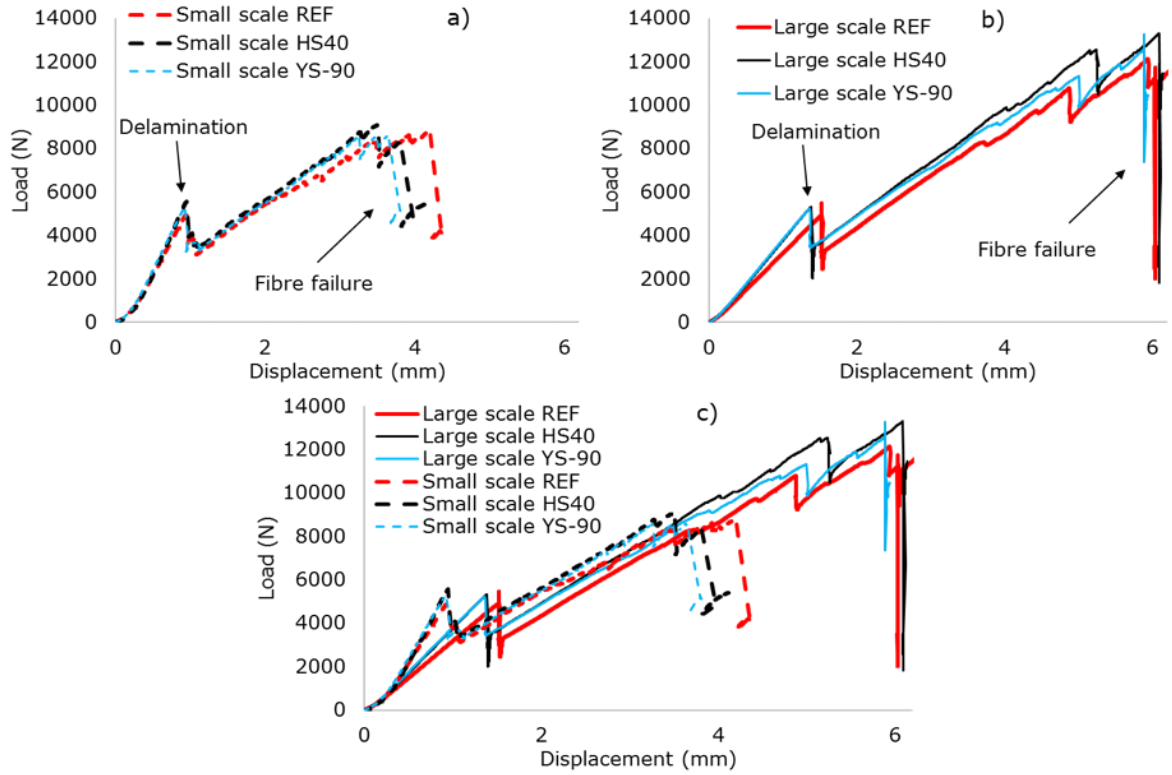

Fig. 7. Load-displacement results for the quasi-static indentation tests for (a) the small scale samples, (b) the large scale samples and (c) all the investigated samples.

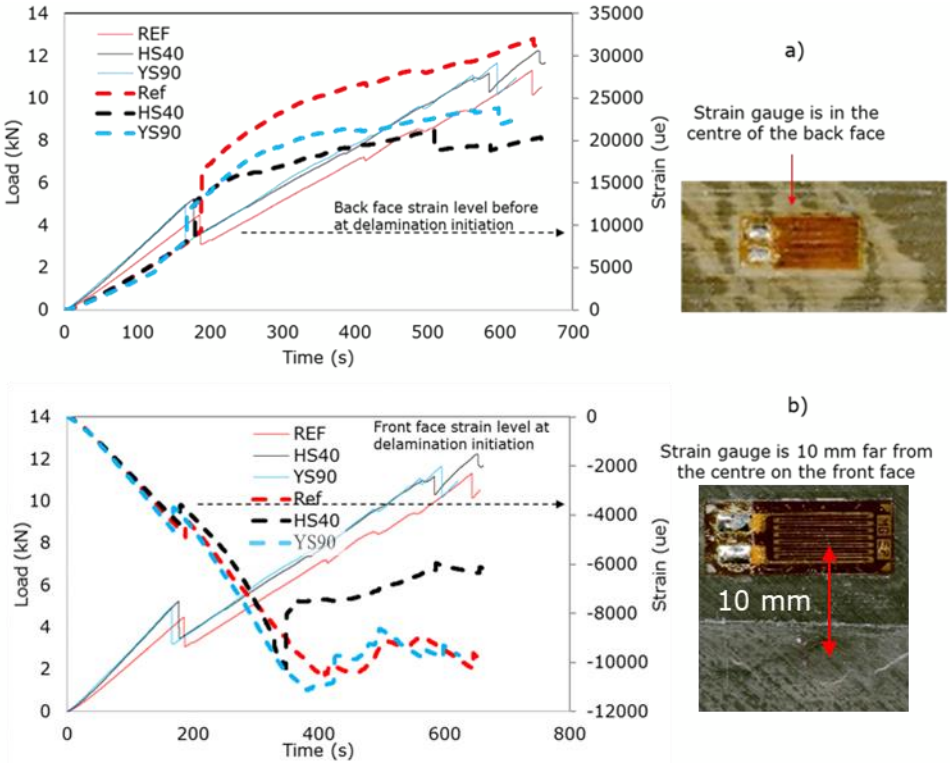

Fig. 8. (a) Back face strain and (b) front face strain, versus time for the indented large scale samples. The dashed lines are representing the strain values and the continuous lines are representing the load values.

The critical energy level that is required for the delamination initiation calculated from the indentation tests is reported in Table 3. The impact energy required to induce the initial delamination in the low-velocity impact in Table 3 was estimated to be 40 % higher than the critical energy level obtained from the indentation test due to the strain-rate sensitivity, as reported for similar tests on a different material [35]. According to Table 3, the sensor-integrated laminates had higher thickness and bending stiffness values than the REF samples. However, their overall load-displacement behaviour is similar, suggesting no significant difference in the indentation behaviour and damage mechanisms of the REF and sensor integrated samples.

Table 3: Energy and stiffness values calculated from the load-displacement graphs.

Sample type	Dimensions (mm)	Thickness (mm)	Initial stiffness (kN/mm)	Absorbed elastic energy before initial delamination, calculated from the area under load-displacement graph (J)	Impact energy required to induce the initial delamination in the low-velocity impact (J)
Small scale REF	70 x 45 x 4.64	4.6	6.073	2.05	2.87
Large scale REF	140 x 90 x 4.64	4.6	3.335	3.41	4.77
Small scale HS40	70 x 45 x 5.05	5.05	6.714	2.15	3.01
Large scale HS40	140 x 90 x 5.05	5.05	4.007	3.38	4.73
Small scale YS90	70 x 45 x 5.05	5.05	6.714	2.15	3.01
Large scale YS90	140 x 90 x 5.05	5.05	4.007	3.38	4.73

4.2. Low-velocity impact results

A series of drop tower tests with different energy levels, starting from energy levels associated with no visible damage and increasing, were performed on the investigated samples. Using the estimated critical elastic energy level obtained in Table 3, the minimum energy level was set to 3 J for the large scale samples. Figure 9 displays the load-displacement plots for the large REF samples subjected to impact at varying energy levels ranging from 3 J to 124 J. The sensor integrated samples showed a similar behaviour as the Reference samples. Fig. 10 compares impact behaviour of the large REF and the sensor integrated samples impacted at 96 J. Similar to the indentation results, for the impacted samples, there is a load drop that is associated with the initiation of delamination. For the large-scale samples, as can be seen from Fig. 9, there is no observed load drop in association with 3 J and 6 J impacts, indicating that these energy levels do not result in any damage to the samples. However, an 8 J impact resulted in a substantial load drop, indicating the initiation of delamination. Based on the load-displacement graphs, it is anticipated that energy levels above 8 J will result in significant damage. Notably, impacts at 64 J, 96 J, and 128 J caused significant load drops due to fibre failure, resulting in a loss of sample integrity and a significant residual deflection.

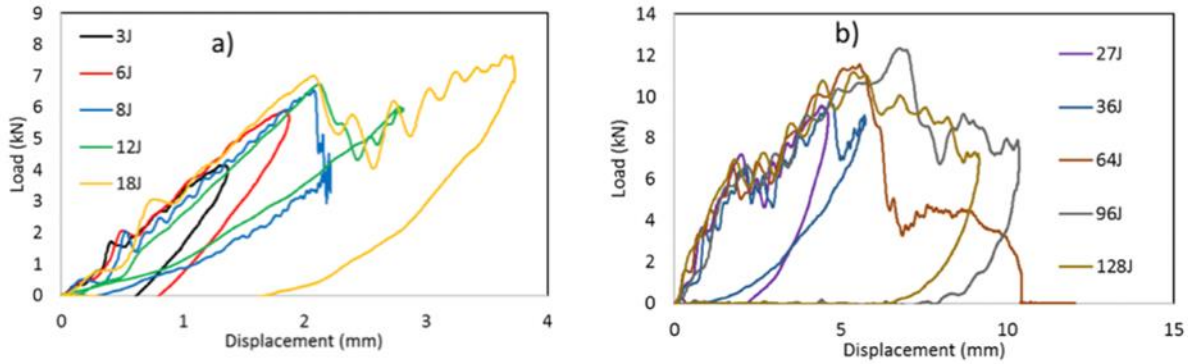

Fig. 9. comparison of load-displacement plots generated from drop-weight impacts on the large scale REF laminates at varying energy levels.

The same energy levels, starting from 3J, was also used for the small scale samples. The impact behaviour of the small scale samples had a similar trend as the large scale samples, however the repeatability of the load-displacement graphs were not as good as the large scale samples. Delamination damage in the small scale samples was observed for the 6 J impact test, while no damage was observed during the 3 J impact test. This implies that a greater percentage of the absorbed elastic energy in indentation testing should be utilized when performing critical impact energy calculations for the small scale samples in Table 3.

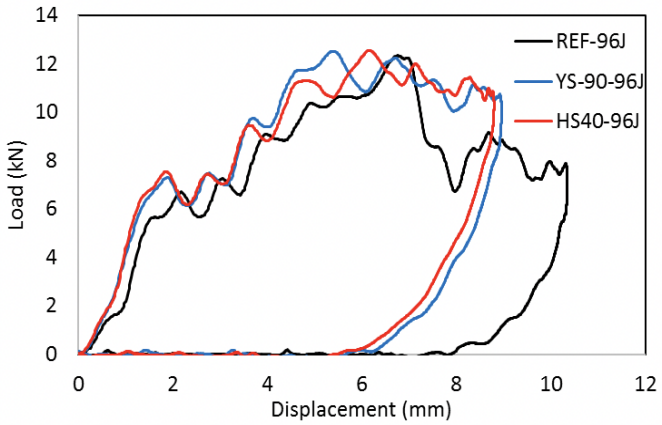

Fig. 10. Comparing the load-displacement plots obtained from the drop-weight impact for the investigated large scale REF laminates impacted at 96J.

By utilizing Equation 7, it is possible to obtain the energy absorbed by the samples over time, expressed as $E_a(t)$. Where V(t) is the velocity, $w_i(t)$ is displacement of the impactor, and g is the acceleration caused by the gravity.

$$E_a(t) = \frac{M_i\left(V_0^2 - V(t)^2\right)}{2} + M_i g w_i(t) \quad (7)$$

Fig. 11 shows comparisons of energy absorption of the Ref samples under different impact energy levels. The higher the damage level is, the higher the energy absorption is expected to be, as evidenced by the higher absorbed impact energy at higher energy levels than the lower energy levels. Fig. 12 illustrates that the large scale samples have a similar absorbed impact energy for the sensor integrated and Ref samples, implying that the damage mechanisms absorbed a similar amount of energy for the given impact energy.

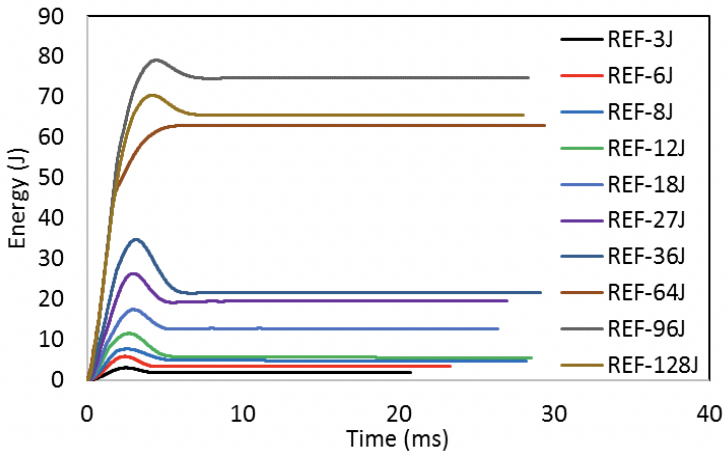

Fig. 11. Comparisons of absorbed energy-time plot obtained from drop-weight impacts on the analysed laminates at varying energy levels.

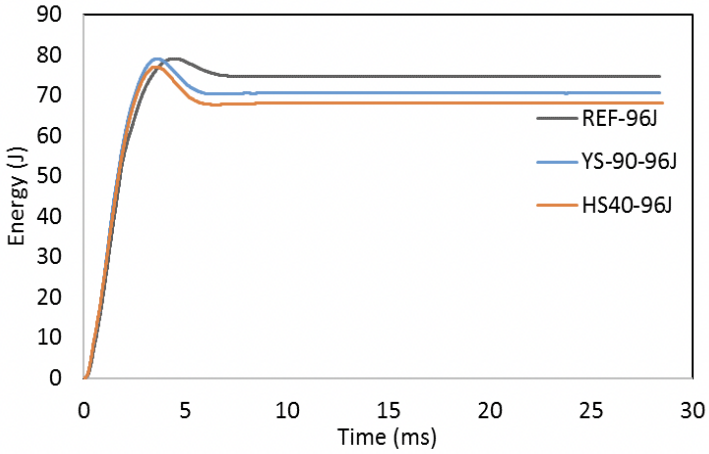

Fig. 12. Comparisons of absorbed energy-time plot obtained from drop-weight impacts on the analysed large scale laminates impacted at 96 J.

4.3 Visual observations and C-scan results

This section analyses the correlation between the internal damage and surface-visible damage caused by the low-velocity impacts. An EPSON scanner, WorkForce DS-70000, was used to take clear images of both the front (impacted) and back face of the samples. Of key interest was the visual appearance change at different energy levels and to compare the size of any visible change with the C-scan results. Fig. 13 shows an example of the EPSON scans and C-scans for the large samples subjected to 12 J. C-scan observations showed that all samples exhibit considerable delamination damage, with the REF sample demonstrating slightly greater delamination size compared to the sensor-integrated samples. Notably, there is no observable change in the appearance of the REF sample on either face. The HS40 sample displays a change in appearance on the front face and slight colour alteration on the back face, however visible colour change is observable for the YS-90 sample on both the front and back faces.

As previously mentioned, these colour changes result from damage induced in the hybrid sensors and a higher level of damage in the sensor was expected in the YS-90 sample compared to the HS40 sample, owing to the lower strain to failure of the YS-90 carbon.

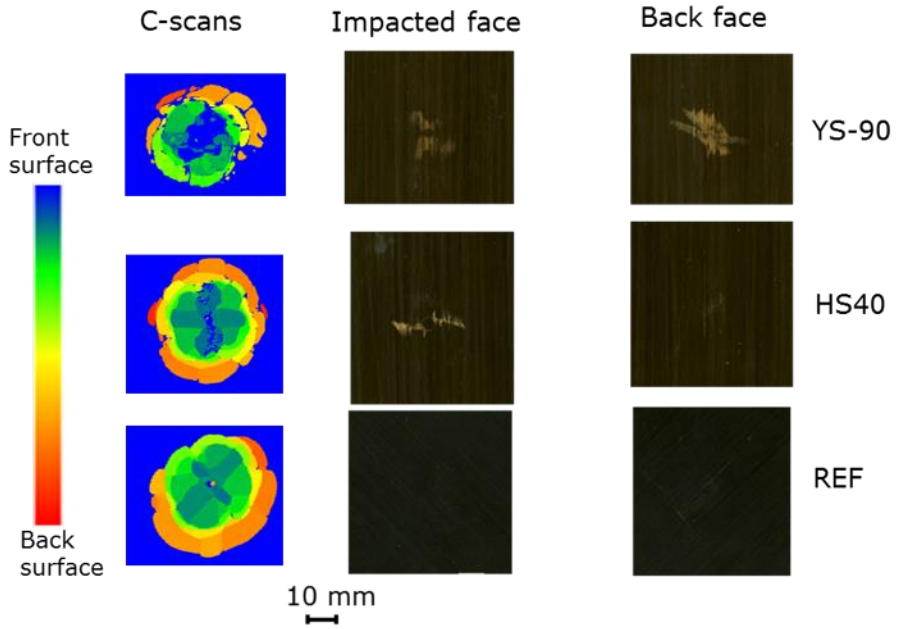

Fig. 13. Images of the impacted samples using EPSON scanner and C-scan, taken from the front face and back face after being subjected to 12 J impact energy.

Similar to Fig. 13, all the impacted samples are EPSON scanned and C-scanned and the results for different configurations and sizes are illustrated in Fig. 14 to Fig. 19. Inspection of the figures reveals that none of the configurations exhibit observable C-scan damage at the 3 J energy level, and BVID delamination, defined as any detectable delamination via C-scan,

initiates at 6 J and 8 J for the small scale and large scale samples, respectively. The C-scan results validate an increasing trend in damage size with increasing impact energy levels. No significant differentiation in indented depth was observed for 32 J and below. However, high-energy levels (above 32 J) resulted in fibre failure and penetration. This is also true for the back face of the large REF samples, where no visible damage was apparent up to 32 J, but higher energy levels resulted in obvious fibre breakage caused by tensile stresses. For the small scale REF samples, the damage in the back and front faces started to happen at an earlier impact energy compared to the large scale REF samples.

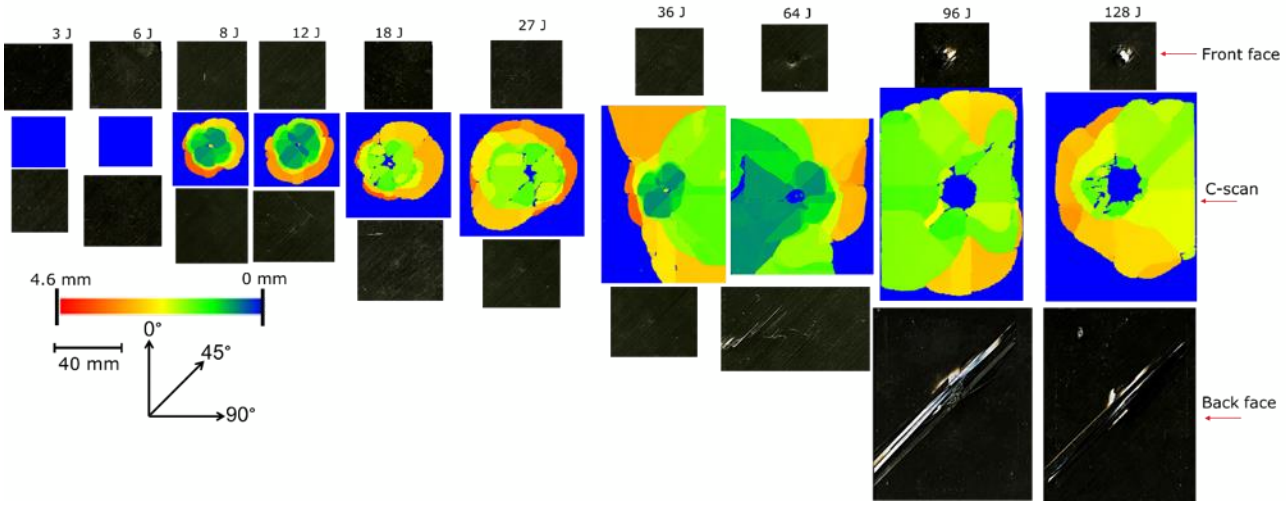

Fig. 14. Images of the large scale REF samples at varying impact energy levels obtained by the C-scanner and the EPSON scanner. The 40 mm scale applies to the in-plane dimensions. The colour scale applies to the location of the c-scanned delamination through the thickness.

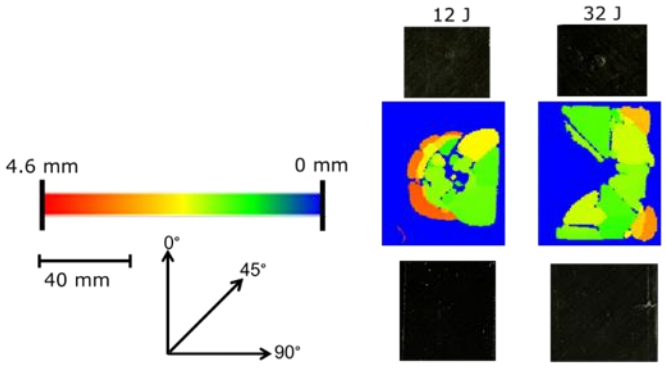

Fig. 15. Images of the small scale REF samples at varying impact energy levels obtained by the C-scanner and the EPSON scanner.

In contrast to the REF samples, there is a visually distinguishable damage on the front and back face of the large and small scale YS-90 samples starting from 6 J (for the small scale sample)

and 8 J (for the large scale sample) which is indicating the existence of the C-scan revealed damage. The final failure for the small scale samples was mainly free-edge delamination, whereas it was fibre failure for the large scale samples. As a result, a slightly different type of visible damage mechanism is observable on the back and front faces when comparing the small and large samples. The HS40 samples behaved similar to the YS-90 samples, however due to the higher strain to failure of the HS40 fibre, the visible surface damage for the HS40 appeared from 27 J (for the small scale sample) and 12 J (for the large scale sample). As shown in Fig. 20, the size of the visible damage increases with higher energy and the C-scans show that the delamination area also increases with increasing impact energy. The high impact levels, >27J, are not illustrated in Fig. 20, as there was no discernible relationship between the concealed delamination area and the visible surface alteration. A larger visible damage is observed in the back face of the YS-90 samples compared with the front face, and the large scale samples showed a larger visible damage than the small scale samples. For the HS40 samples, only the large scale samples showed visible damage at the front face in the low energy levels, and no visible damage is observed on the back face or small scale samples up until significant internal delamination. The difference between the YS90 and HS40 samples is the type of sensing carbon fibre prepreg used, which shows the high level of dependency of BVID detection sensors on the sensing material's strain to failure. The size of the sample, and consequently the in-plane to thickness size ratio is another important factor for the sensor design. The higher this ratio is, the lower the visual sensor activation threshold is.

In a conventional laminated composite, mid-plane delamination usually occurs earlier than the other types of damage, causing BVID. Using equations 1, 2 and 5, the load level required for the initiation of the back-face tensile fibre failure and impacted side failure of the sensor material can be designed to be lower than the mid-plane delamination initiation. This can be done by selecting appropriate materials and layup for the hybrid composite sensor to fail below the predefined impact energy levels. Depending on the application, the accessible side of the composite plate can be the impacted side, e.g. an aircraft skin, or the back face, e.g. pressure vessels with internal impact events. Further research on the development of analytical and finite element-based design tools is required to explore the effective parameters in the hybrid sensor design and to identify the target sensor material properties and architectures for a range of substrate material properties, thicknesses, and in-plane dimensions.

Another critical point on the effectiveness of the proposed hybrid composite is the effect of integrated sensors on residual compression after impact strength. Compression after the impact tests were conducted on the investigated samples, and the sensor-integrated laminates showed

some improvements in the compression after impact strength compared to the reference laminates. However, this improvement was marginal and not conclusive, therefore the results are not reported in this paper, and further research is required to improve this understanding.

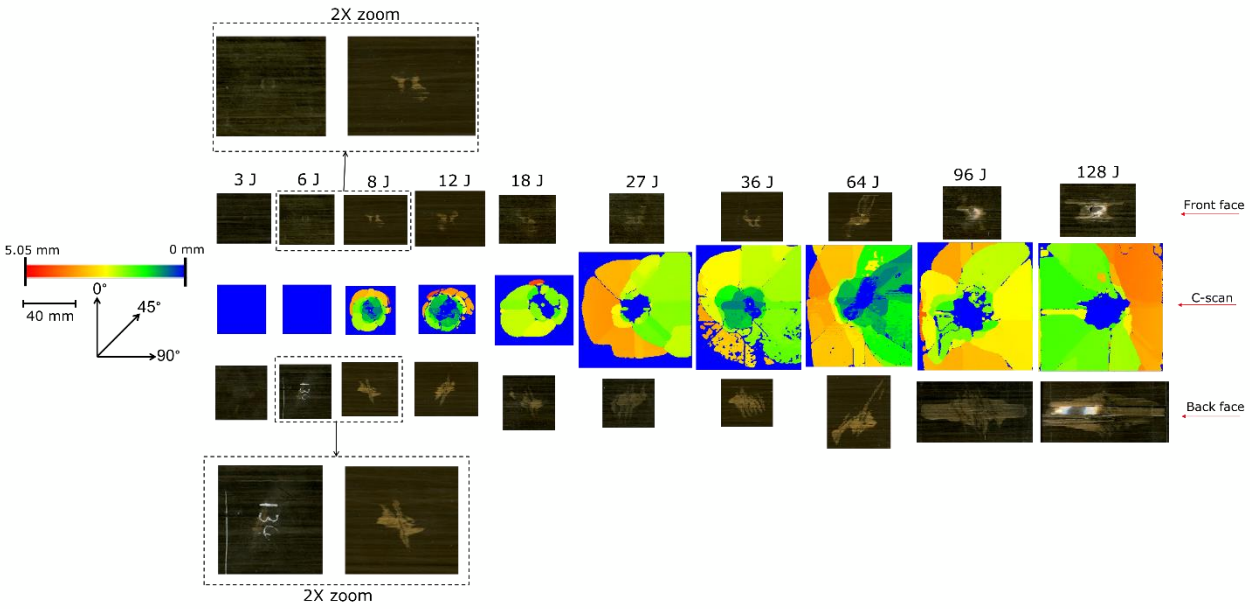

Fig. 16. Images of the large scale YS-90 samples at varying impact energy levels obtained by the C-scanner and the EPSON scanner.

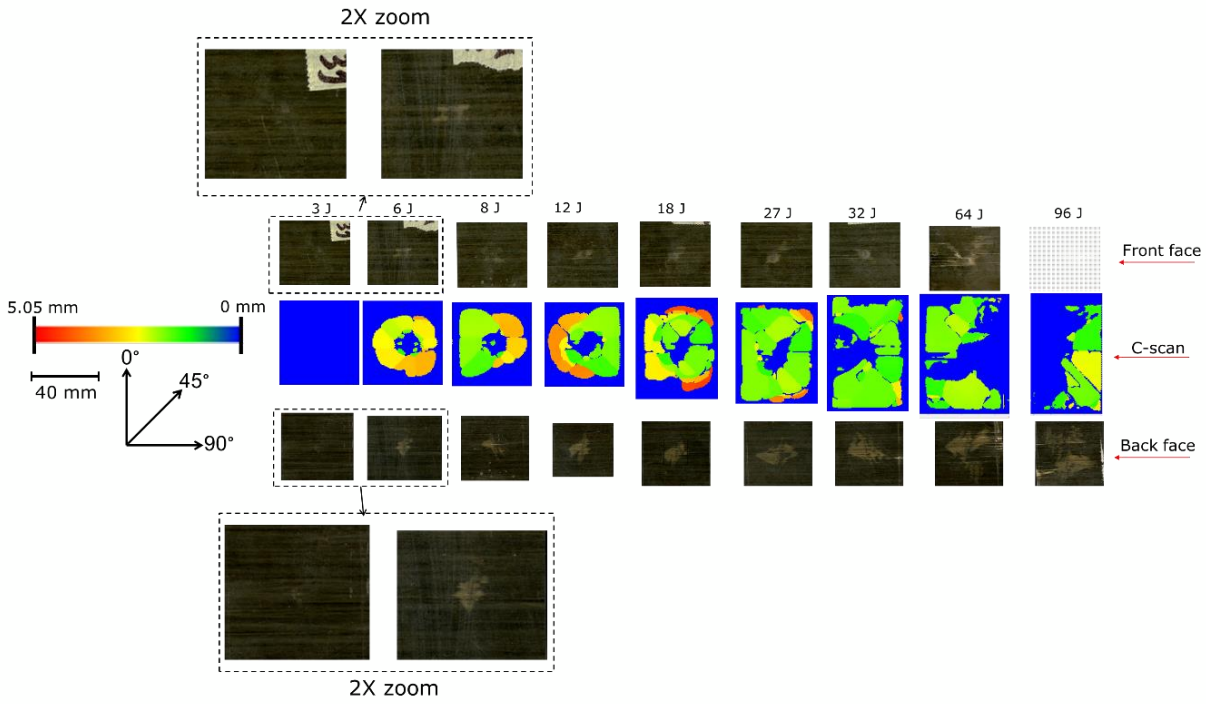

Fig. 17. Images of the small scale YS-90 samples at varying impact energy levels obtained by the C-scanner and the EPSON scanner.

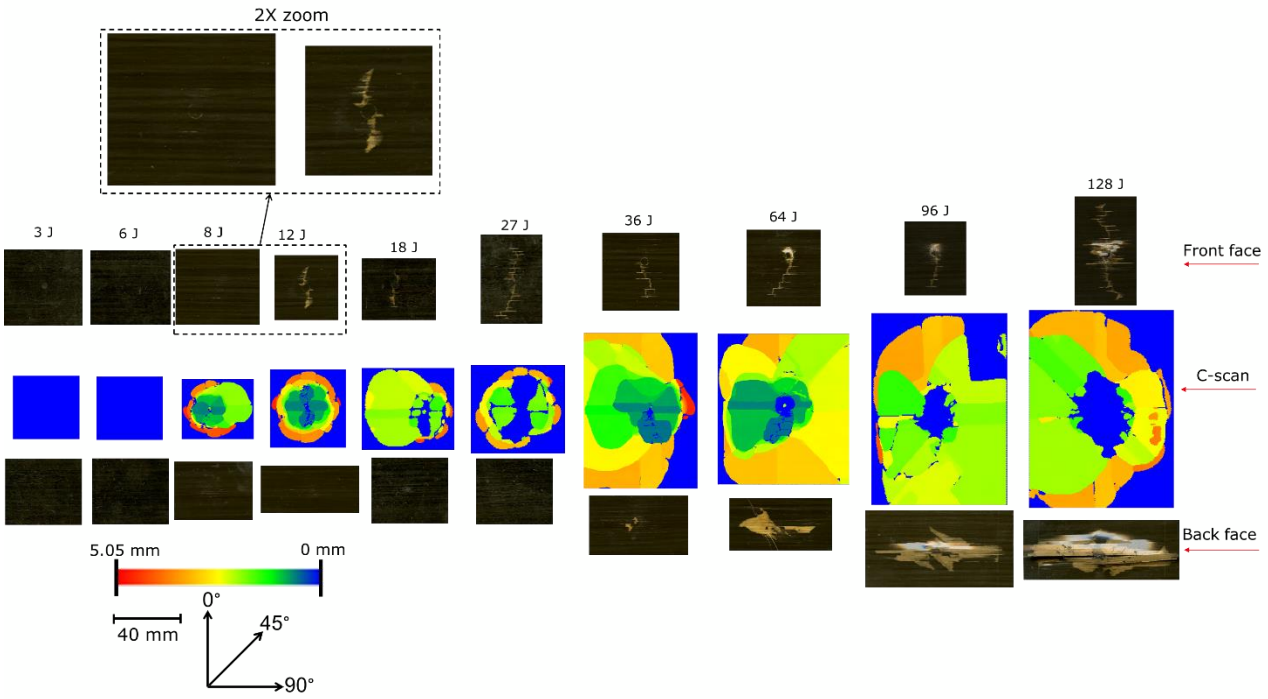

Fig. 18. Images of the large scale HS40 samples at varying impact energy levels obtained by the C-scanner and the EPSON scanner.

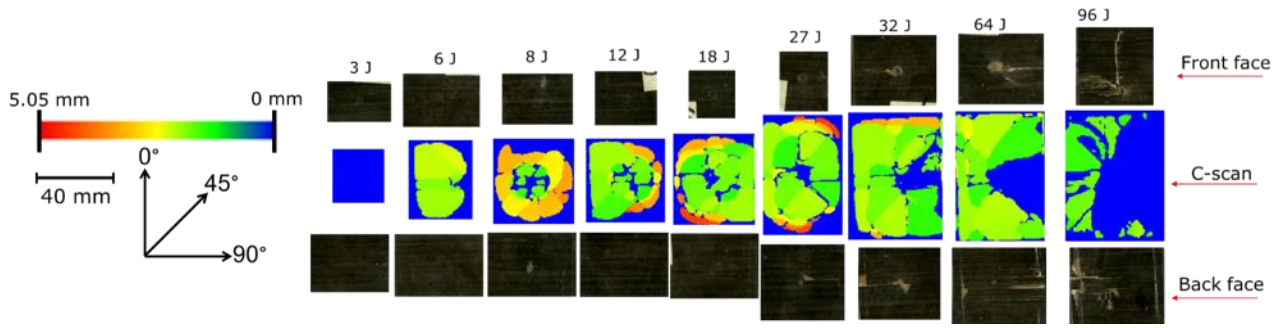

Fig. 19. Images of the small scale HS40 samples at varying impact energy levels obtained by the C-scanner and the EPSON scanner.

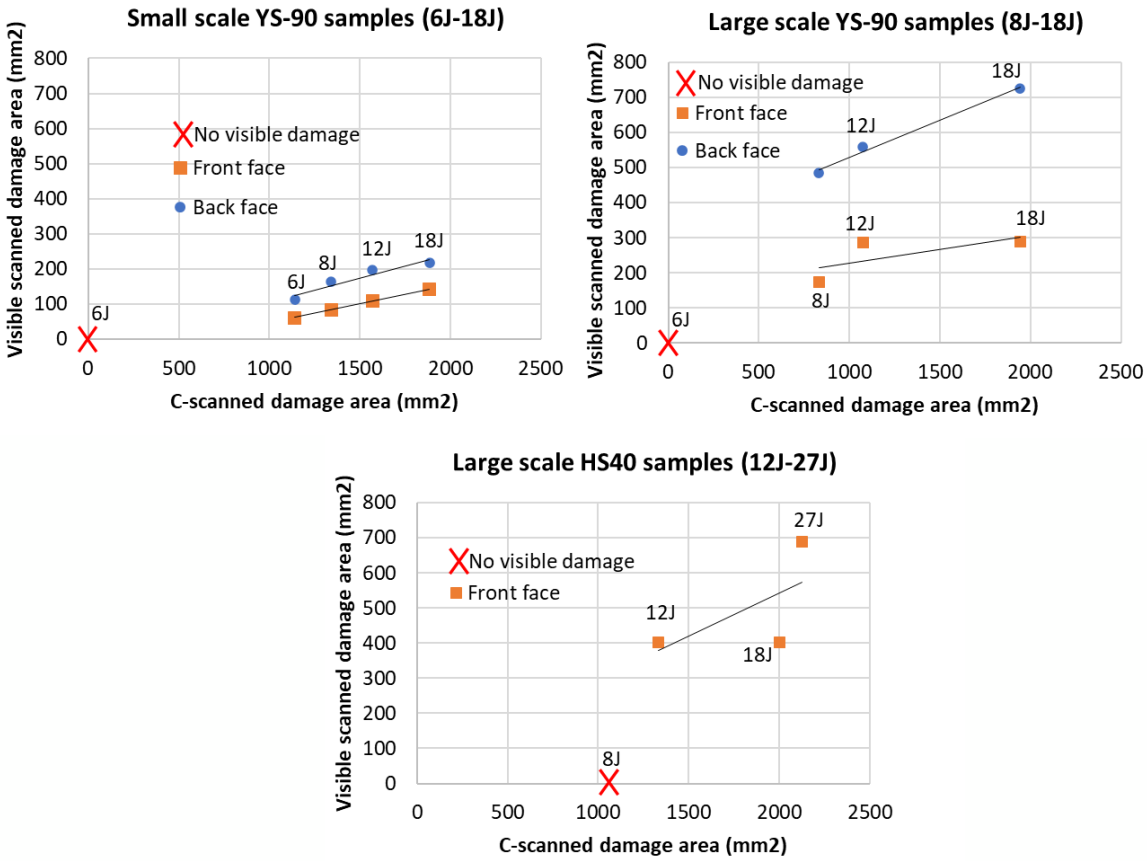

Fig. 20. C-scanned damaged area versus visible scanned damage area for the investigated samples.

4.4 Future work

Future research is required to understand the competition between the low-velocity impact-induced damage in the sensor and substrate laminate and to optimise the damage scenario to increase the visibility of the sensor-related damage and to improve residual compression after impact strength. Therefore, advanced experimentally validated FEM is proposed to develop the understanding and design optimization in a timely and cost-effective way for different sizes and curvature samples under various impactor shapes representing real-world conditions. In addition, FEM can help establish a link between surface damage and residual strength for complex shapes and geometries which might be costly or difficult to do experimentally.

5. Conclusion

Novel hybrid composite sensors were proposed to detect damage in carbon/epoxy laminated composites, and the following conclusions are drawn.

- The introduced novel hybrid sensors can produce composites with self-sensing ability to indicate damage. C-scan images of the investigated samples showed the existence of

damage with an increasing trend in size with the rise in impact energy level. For the samples without the sensing layer (REF), despite the existence of significant delamination damage for the samples impacted up to 32J, no visible damage was seen on the samples' surface by the naked eye. However, for the high impact energy levels, significant fibre failure was observed in the front and back faces of the REF samples. Whereas for the laminates covered with the sensing layers, there was visible damage both in the front and back faces, from the low energy levels indicating the existence of the damage. The system developed is quite useful for early indication of damage and improving probability of detection in carbon/epoxy composite structures.

- The performance of the integrated sensor highly depends on the material properties of the sensor, and the in-plane to thickness size ratio of the impacted laminate. Both of these parameters significantly impact the correlation between the extent of internal damage (delamination) and the visible surface damage on composite panels when subjected to low-velocity impacts. Relationships were clearly visible, for impact energies lower than the ones that cause fibre failure, with increasing visible damage area correlating to increasing area of internal delamination. However, for the high impact levels, >27J, there was no discernible relationship between the concealed delamination area and the visible surface alteration. Consequently, the hybrid composite sensors are most effective for low-energy impacts where the lack of visibility of damage is a significant obstacle. The visibility of impact damage can be customized by selecting suitable sensing material properties and calibrating the sensor to the substrate's in-plane dimensions and material properties.

Acknowledgements

The research presented in this paper was financially supported by the UK Engineering and Physical Sciences Research Council (EPSRC) Grants EP/V009451/1, which focused on the development of high-performance impact-resistant composites with visible damage, and EP/I02946X/1, which aimed to advance high-performance ductile composite technology in collaboration with Imperial College. All data necessary to support the conclusions of this study are provided within the paper.

References

1. McAdam, R., O'Hare, T. and Moffett, S., 2008. Collaborative knowledge sharing in composite new product development: an aerospace study. Technovation, 28(5), pp.245-256.

2. Siow, Y.P. and Shim, V.P.W., 1998. An experimental study of low velocity impact damage in woven fiber composites. Journal of Composite Materials, 32(12), pp.1178-1202.

3. Lopes, C.S., Camanho, P.P., Gürdal, Z., Maimí, P. and González, E.V., 2009. Low-velocity impact damage on dispersed stacking sequence laminates. Part II: Numerical simulations. Composites Science and Technology, 69(7-8), pp.937-947.

4. Adsit, N.R. and Waszczak, J.P., 1979. Effect of near-visual damage on the properties of graphite/epoxy (pp. 101-117). ASTM International.

5. Dafydd, I. and Sharif Khodaei, Z., 2020. Analysis of barely visible impact damage severity with ultrasonic guided Lamb waves. Structural Health Monitoring, 19(4), pp.1104-1122.

6. Bossi, R.H. and Georgeson, G.E., 2020. Nondestructive testing of aerospace composites. In Polymer Composites in the Aerospace Industry (pp. 461-489). Woodhead Publishing.

7. Towsyfyan, H., Biguri, A., Boardman, R. and Blumensath, T., 2020. Successes and challenges in non-destructive testing of aircraft composite structures. Chinese Journal of Aeronautics, 33(3), pp.771-791.

8. Cook, L., Bellamy, P., Boulic, A., Harris, D. and Irving, P.E., 2013. Reliability of damage detection in advanced composite aircraft structures. TSO (The Stationery Office).

9. Silberschmidt, V.V. ed., 2016. Dynamic deformation, damage and fracture in composite materials and structures. Woodhead Publishing.

10. The International Air Transport Association (IATA) Safety Report, AERO_Q207_article3.pdf (boeing.com).

11. Your guide to general visual inspections of aircraft | Mainblades

12. Abisset, E., Daghia, F., Sun, X.C., Wisnom, M.R. and Hallett, S.R., 2016. Interaction of inter-and intralaminar damage in scaled quasi-static indentation tests: Part 1–Experiments. Composite Structures, 136, pp.712-726.

13. Saeedifar, M., Najafabadi, M.A., Zarouchas, D., Toudeshky, H.H. and Jalalvand, M., 2018. Barely visible impact damage assessment in laminated composites using acoustic emission. Composites Part B: Engineering, 152, pp.180-192.

14. Meehan, D.G., Wang, S. and Chung, D.D.L., 2010. Electrical-resistance-based sensing of impact damage in carbon fiber reinforced cement-based materials. Journal of Intelligent Material Systems and Structures, 21(1), pp.83-105.

15. Kinet, D., Mégret, P., Goossen, K.W., Qiu, L., Heider, D. and Caucheteur, C., 2014. Fiber Bragg grating sensors toward structural health monitoring in composite materials: Challenges and solutions. Sensors, 14(4), pp.7394-7419.
16. Tabatabaeian, A., Liu, S., Harrison, P., Schlangen, E. and Fotouhi, M., 2022. A review on self-reporting mechanochromic composites: An emerging technology for structural health monitoring. Composites Part A: Applied Science and Manufacturing, p.107236.
17. Blaiszik, B.J., Kramer, S.L., Olugebefola, S.C., Moore, J.S., Sottos, N.R. and White, S.R., 2010. Self-healing polymers and composites. Annual review of materials research, 40(1), pp.179-211.
18. Diesendruck, C.E., Sottos, N.R., Moore, J.S. and White, S.R., 2015. Biomimetic self-healing. Angewandte Chemie International Edition, 54(36), pp.10428-10447.
19. Calvino, C., Neumann, L., Weder, C. and Schrettl, S., 2017. Approaches to polymeric mechanochromic materials. Journal of Polymer Science Part A: Polymer Chemistry, 55(4), pp.640-652.
20. Patrick, J.F., Robb, M.J., Sottos, N.R., Moore, J.S. and White, S.R., 2016. Polymers with autonomous life-cycle control. Nature, 540(7633), pp.363-370.
21. Caruso, M.M., Davis, D.A., Shen, Q., Odom, S.A., Sottos, N.R., White, S.R. and Moore, J.S., 2009. Mechanically-induced chemical changes in polymeric materials. Chemical reviews, 109(11), pp.5755-5798.
22. Jalalvand, M., Fuller, J., Wisnom, M.R. and Czél, G., 2019. A simple and robust approach for visual overload indication-UD thin-ply hybrid composite sensors. Composites Part A: Applied Science and Manufacturing, 121, pp.376-385.
23. Civera, M. and Surace, C., 2022. Non-Destructive Techniques for the Condition and Structural Health Monitoring of Wind Turbines: A Literature Review of the Last 20 Years. Sensors, 22(4), p.1627.
24. Davies, G.A. and Zhang, X., 1995. Impact damage prediction in carbon composite structures. International Journal of Impact Engineering, 16(1), pp.149-170.
25. Olsson R, Nilsson S, 2006. Simplified prediction of stresses in transversely isotropic composite plates under Hertzian contact load, Composite Structures 73, pp. 70–77.
26. Lechnitskii SG., 1981. Theory of elasticity of an anisotropic body (translation of revised 1977 Russian edition). Moscow: Mir Publishers; [Chapter 9].
27. Fotouhi, S., Khayatzadeh, S., Pui, W.X., Damghani, M., Bodaghi, M. and Fotouhi, M., 2021. Detection of barely visible impact damage in polymeric laminated composites using a biomimetic tactile whisker. Polymers, 13(20), p.3587.

28. Wu, X. and Wisnom, M.R., 2023. Compressive failure strain of unidirectional carbon fibre composites from bending tests. Composite Structures, 304, p.116467.
29. Fotouhi, M., Jalalvand, M. and Wisnom, M.R., 2017. High performance quasi-isotropic thin-ply carbon/glass hybrid composites with pseudo-ductile behaviour in all fibre orientations. Composites Science and Technology, 152, pp.101-110.
30. Fotouhi, M., Jalalvand, M., Prato, A. and Wisnom, M.R., 2020, December. Thin ply carbon/glass hybrid laminates to activate new damage mechanisms under indentation. European Conference on Composite Materials, ECCM.
31. Fotouhi, M., Jalalvand, M., Saeedifar, M., Xiao, B. and Wisnom, M.R., 2020. High performance quasi-isotropic thin-ply carbon/glass hybrid composites with pseudo-ductile behaviour loaded off-axis. Composite Structures, 247, p.112444.
32. Czél, G., Jalalvand, M. and Wisnom, M.R., 2014, June. Development of pseudo-ductile hybrid composites with discontinuous carbon-and continuous glass prepregs. In Proceedings of ECCM-16 conference. Seville.
33. ARAI, Y., 2001. Pitch-based carbon fiber with low modulus and high heat conduction. Nippon steel technical report. Overseas, (84), pp.12-17.
34. ASTM D7136/D7136M-12, 2012. Standard test method for measuring the damage resistance of a fiber-reinforced polymer matrix composite to a drop-weight impact event.
35. Sun, X.C. and Hallett, S.R., 2017. Barely visible impact damage in scaled composite laminates: Experiments and numerical simulations. International Journal of Impact Engineering, 109, pp.178-195.